

Effect of Mn(II) on the Structure and Reactivity of Biogenic Uraninite

HARISH VEERAMANI,[†]
 ELEANOR J. SCHOFIELD,[‡]
 JONATHAN O. SHARP,^{§,†}
 ELENA I. SUVOROVA,[†]
 KAI-UWE ULRICH,^{||} APURVA MEHTA,[‡]
 DANIEL E. GIAMMAR,^{||} JOHN R. BARGAR,[‡]
 AND RIZLAN BERNIER-LATMANI^{†,*}

Environmental Microbiology Laboratory, École Polytechnique Fédérale de Lausanne, Lausanne, CH 1015, Switzerland, Stanford Synchrotron Radiation Lightsource, 2575 Sand Hill Rd., Menlo Park, California 94025, and Department of Energy, Environmental and Chemical Engineering, Washington University, One Brookings Drive, St. Louis, Missouri 63130

Received May 12, 2008. Revised manuscript received June 11, 2009. Accepted July 6, 2009.

The efficacy of a site remediation strategy involving the stimulation of microbial U(VI) reduction hinges in part upon the long-term stability of the product, biogenic uraninite, toward environmental oxidants. Geological sedimentary uraninites (nominal formula UO_2) reportedly contain abundant cation impurities that enhance their resistance to oxidation. By analogy, incorporation of common groundwater solutes into biogenic uraninite could also impart stability-enhancing properties. Mn(II) is a common groundwater cation, which has a favorable ionic radius for substitution reactions. The structure and reactivity of Mn(II)-reacted biogenic uraninite are investigated in this study. Up to 4.4 weight percent Mn(II) was found to be structurally bound in biogenic uraninite. This Mn(II) incorporation was associated with decreasing uraninite particle size and structural order. Importantly, the equilibrium solubility of Mn-reacted uraninite was halved relative to unreacted uraninite, demonstrating changes in thermodynamic properties, while the dissolution rate was up to 38-fold lower than that of unreacted biogenic uraninite. We conclude that structural incorporation of Mn(II) into uraninite has an important stabilizing effect, leading to the prediction that other groundwater solutes may similarly stabilize biogenic uraninite.

Introduction

In situ reductive biotransformation of subsurface U(VI) contamination has been extensively researched as a method to immobilize uranium because of the relative insolubility of its reduced form (1). A significant issue associated with uranium bioremediation is the susceptibility of biogenic uraninite, the product of microbial U(VI) reduction (2), to chemical oxidation by O_2 (3–5), nitrite (6), nitrate (4), and

Fe(III) (hydr)oxides (7) and to biological oxidation coupled with nitrate reduction (8).

For effective long-term bioimmobilization of uranium, biogenic uraninite should exhibit slow kinetics of reoxidation. Consequently, strategies for reductive immobilization of U should include considerations for preventing or minimizing its oxidative remobilization. The UO_2 structure can accommodate excess oxygen and cation impurities without compromising the cubic unit cell (9). Indeed, the term “uraninite” refers to the nonstoichiometric and cation-substituted forms of UO_2 found ubiquitously in natural settings (10). Cation impurities reported in sedimentary uraninites include Ca^{2+} and Pb^{2+} . These cations are thought to occur as lattice substituents for U^{4+} with charge balance provided by higher-valent U (hyperstoichiometry) and/or excess oxygens (11).

Nonstoichiometry and cation substitution have been credited with increased uraninite stability with respect to oxidation and corrosion (10–12). This behavior is of considerable pragmatic and fundamental significance to bioremediation efforts, particularly considering that the stimulation of metal bioreduction in the subsurface will result in anoxic and reducing groundwaters rich in potential cation substituents such as Mn^{2+} or Fe^{2+} .

The study focuses on Mn(II) because of its ubiquity in groundwater, where it is found at concentrations up to 0.1 mM [Rifle Integrated Field-Scale Subsurface Research Challenge (IFC) Site] (13) or up to 4 mM [Oak Ridge Field Research Center (FRC)] (13, 14). These values are expected to be even higher during bioremediation, where reductive dissolution of Mn oxides significantly escalates dissolved Mn(II). Moreover, the ionic radius of cubically coordinated Mn^{2+} (0.93 Å) is slightly smaller than that of U^{4+} (1.00 Å) (15), and thus Mn^{2+} should readily fit into the uraninite lattice. The goal of the present study was to assess whether U(VI) reduction in the presence of soluble Mn(II) could lead to structural binding within biogenic uraninite and to evaluate the impact on uraninite particle size, structure, and reactivity.

Distinguishing internal structural binding of impurity cations in a host (i.e., doping) from other mechanisms of association such as adsorption at surfaces or precipitation of intermixed phases is nontrivial and requires aqueous and structural characterization techniques. In this study, we have coupled sorption, washing, and digestion techniques with investigations of molecular scale structure, solubility, and dissolution kinetics to develop a holistic model of this complex biogenic material.

Materials and Methods

Reduction of U(VI) in the Presence of Mn. The reduction of U(VI) by *Shewanella oneidensis* MR-1 was carried out at pH 6.3 (16) except that, during the production of Mn-reacted uraninite, a small amendment from a sterile, anaerobic stock (1 M) of $MnCl_2$ (Aldrich) was made prior to the addition of an aliquot of anaerobic stock (10 mM) uranyl acetate (Fluka). A detailed description is provided in section SI-A of the Supporting Information. Mn-reacted and unreacted uraninite are defined as uraninite produced in the presence of Mn(II) and in its absence, respectively. The biogenic uraninite collected was subjected to a NaOH treatment to remove the biomass and sorbed U(IV) as described previously (16) and in section SI-B of the Supporting Information. Uraninite that has been subjected to a NaOH treatment is referred to as NaOH-treated uraninite. NaOH-treated uraninite was stored at circumneutral pH in anaerobic Milli-Q water and was the primary material used for U X-ray absorption spectroscopy (XAS), synchrotron powder diffraction (SR-PD), electron

* Corresponding author phone: 41 21 693-5001; fax: 41 21 693-6205; e-mail: rizlan.bernier-latmani@epfl.ch.

[†] École Polytechnique Fédérale de Lausanne.

[‡] Stanford Synchrotron Radiation Lightsource.

[§] Present address: Environmental Science and Engineering Division, Colorado School of Mines, 1500 Illinois St., Golden, Colorado 80401.

^{||} Washington University.

TABLE 1. Characteristics of NaOH-Treated and Mn-Reacted Uraninite^a

Mn concentration (mM)	Mn in UO ₂ (mg/g)		mean particle size (±0.15 nm)	Mn atoms per particle	U atoms per particle
	after NaOH treatment	after pH 5 wash			
8	85.8 ± 4.0	30.4 ± 1.4	1.7 nm	8.1	54.4
5	81.6 ± 3.6	32.8 ± 1.7	1.9 nm	14.7	91.1
2.5	84.1 ± 3.7	44.4 ± 2.5	—	—	—
1	65.8 ± 3.0	36.1 ± 2.0	2.2 nm	24.7	139.3
0.5	62.9 ± 2.6	36.6 ± 1.8	—	—	—
0.25	68.7 ± 3.7	30.2 ± 1.5	—	25.2	139.8
0.1	—	—	2.2 nm	—	—
0	—	—	2.5 nm	—	—

^a Mn content prior to and after washing at pH 5, HRTEM-determined mean particle size after NaOH treatment but prior to pH 5 washing (error ± 0.15 nm), and calculated average number of Mn and U atoms per particle after pH 5 wash. Dashes correspond to conditions for which no data are available.

microscopy (EM), and continuous flow dissolution analyses. The surface area of the NaOH-treated material was determined to be 50.14 m²/g. A complete list of the 20 samples prepared, along with the treatments and analyses to which each was subjected, is available in Table SI-1 of the Supporting Information.

Acid Digestion of Uraninite. In order to measure the amount of Mn associated with uraninite, an aliquot of the NaOH-treated mineral was centrifuged, and the pellet was resuspended aerobically in 2 mL of concentrated HNO₃. The suspension was placed on a rotary shaker overnight for complete dissolution. The acid digest was analyzed for U(VI) content by kinetic phosphorescence analysis (KPA-11A, Chemchek Instruments) and for dissolved Mn by inductively coupled plasma optical emission spectrometry (ICP-OES, PerkinElmer Plasma 2000) or high-resolution ICP-mass spectrometry (HR-ICP-MS, Thermo Finnigan Element II).

Sorption of Mn(II) onto Uraninite. The sorption behavior of Mn(II) onto biogenic, NaOH-treated uraninite was quantified. Duplicate polypropylene tubes, containing 10 mL of 0.01 M NaCl in O₂-free Milli-Q water preadjusted to pH values ranging from 3 to 10, were amended with uraninite (0.1 g/L) and then 1 mM Mn(II). When necessary, pH was adjusted using 0.5 M HCl or 0.5 M NaOH. Appropriate controls [no Mn(II) or no uraninite] were included to account for the precipitation of Mn or the dissolution of uraninite. The tubes were equilibrated while shaking over 24 h, and the final pH was measured. Samples were filtered using 0.2 μm polyethersulfone (PES) filters and analyzed for Mn and U as above.

Electron Microscopy and X-ray Absorption Spectroscopy. High resolution transmission electron microscopy was carried out as described elsewhere (16) and in section SI-D of the Supporting Information.

U L_{III} edge extended X-ray absorption fine structure (EXAFS) spectra were measured as previously described (ref 16 and section SI-E of the Supporting information). Mn EXAFS samples were loaded in a polycarbonate sample holder with Kapton windows. Fluorescence-yield Mn K-edge EXAFS were collected at room temperature at Stanford Synchrotron Radiation Laboratory (SSRL) beamline 11-2 using Si (220) double-crystal monochromators detuned by 40% to attenuate harmonic intensity and a Canberra 30 element array Ge detector. The monochromator was calibrated with a metallic Mn foil.

Flow-Through Dissolution of Mn-Reacted Uraninite. Continuous-flow stirred tank reactors (CFRs) were used to compare the stability of NaOH-treated, unreacted, and Mn(II)-reacted (5 mM Mn) biogenic uraninite. The 5 mM Mn-reacted sample was selected because it was representative of Mn incorporation in other samples (Table 1). Duplicate CFRs (12.6 mL volume) were loaded with a suspension of biogenic uraninite (approximately 1 g/L) in the anaerobic

chamber and sealed with a filter membrane of 25 nm pore diameter that allows water but not solids to flow through. The CFRs were fed with degassed ultrapure water buffered at pH 7.5 with 5 mM HEPES for anoxic conditions. For oxic experiments, the influent was purged with technical air and contained 1 mM NaHCO₃. A peristaltic pump fed the influent at 2.2 mL/min, and the effluent was analyzed for U and Mn by ICP-MS (Agilent 7500ce). More experimental details are provided in section SI-G of the Supporting Information.

To determine the equilibrium solubility of unreacted and Mn-reacted uraninite, we performed the following operations: The flow in a CFR that had been running under reducing conditions for ~40 residence times was stopped. Closed reactors were operated in stirred batch reactor (SBR) mode in the anaerobic chamber for four days. The dissolved uranium concentration was analyzed. All experiments were carried out at room temperature (20 ± 1 °C) and in the dark. The calculation of dissolution rates from the data is detailed in the SI-H section of the Supporting Information.

Results and Discussion

Aqueous Chemical Behavior: Sorption and Incorporation of Mn into Uraninite. To produce Mn-reacted biogenic uraninite, we carried out the reduction of U(VI) using *S. oneidensis* at different aqueous Mn(II) concentrations. While the reduction was complete within 12 h for most of the conditions, it lasted over 48 h in the presence of 5 and 8 mM Mn(II) (Figure SI-1 of the Supporting Information). Although there are no known ternary complexes of Mn, U, and carbonate, the impact that higher Mn²⁺ concentrations have on the rate of U(VI) reduction is analogous to that of Ca²⁺ additions (17). This suggests a possible inhibitory mechanism involving Mn complexes similar to the Ca–U–CO₃ complexes responsible in the case of Ca (17).

The association of Mn(II) with uraninite is evident from the measurement of Mn and U in acid digests of NaOH-treated, Mn-reacted uraninite (Table 1). In order to spectroscopically differentiate between Mn(II) adsorbed onto uraninite surfaces and internally bound Mn(II), adsorbed Mn(II) was removed by repeated washing at pH 5 (section SI-C of the Supporting Information). Sorption of Mn(II) to preformed, Mn-free, NaOH-treated biogenic uraninite identified pH 5 as an appropriate pH value that minimized Mn(II) sorption and uraninite dissolution (Figure SI-2A,B of the Supporting Information). Mn(II) adsorbed onto uraninite during production and subsequent NaOH washing should be released after five successive 1 h pH 5 washes (Figure SI-3 of the Supporting Information), but Mn(II) bound within uraninite will not be released. Hereafter, NaOH-treated uraninite that was washed at pH 5 will be referred to as pH 5-washed uraninite.

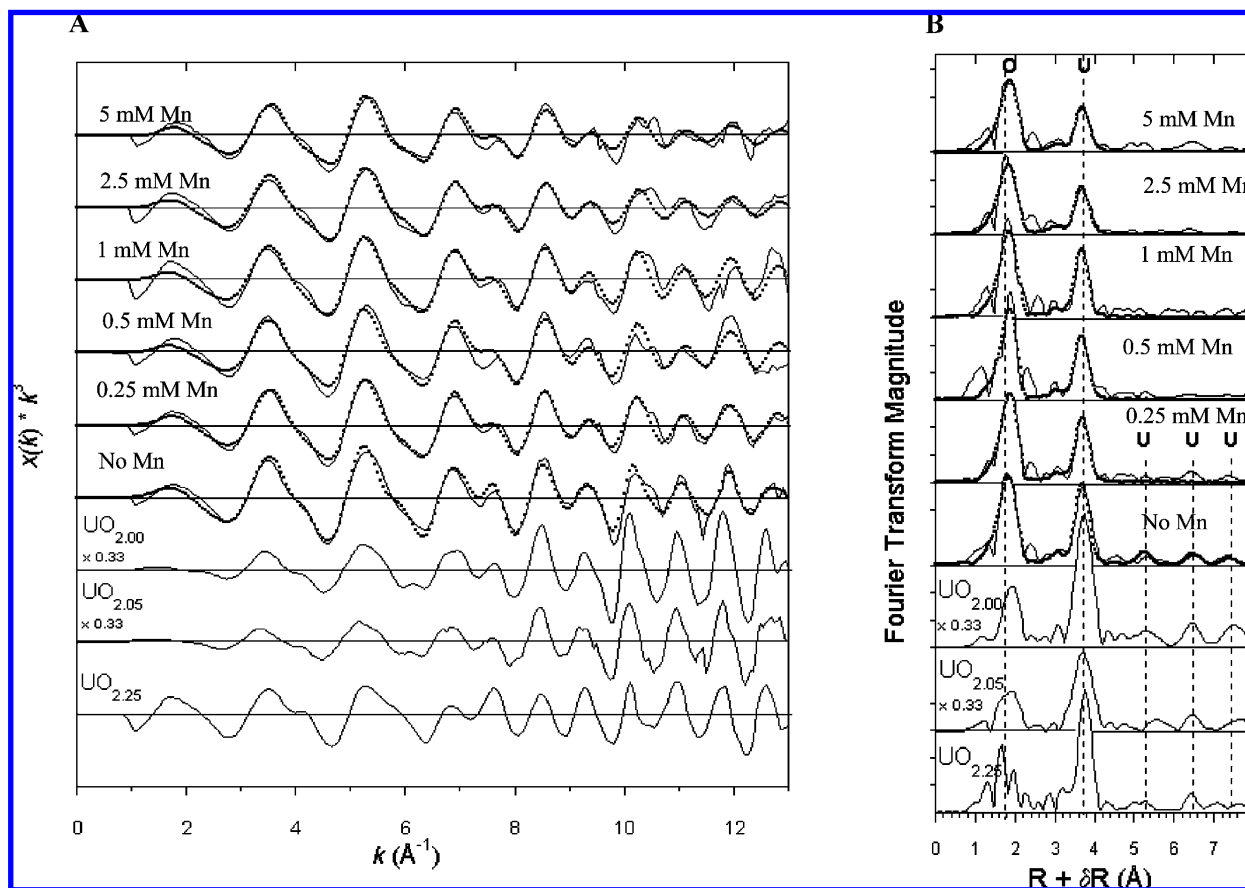


FIGURE 1. U L_{III}-edge spectra for abiotic and NaOH-treated biogenic uraninite. Concentration of Mn at which the uraninites were prepared is indicated. (A) U L_{III} EXAFS spectra (solid lines) with fits to data (dashed lines). (B) Corresponding Fourier transforms.

The fraction of Mn removed by pH 5 washes ranged from 41 to 65% of the total Mn associated with uraninite (description in section SI-C of the Supporting Information). The remainder of Mn(II) (about 3–4.4 wt % of the uraninite) is inferred to be localized within the uraninite particles. This concentration is similar to that reported for Pb (7.4–18.5 wt %) associated with geological uraninites (11, 12). Because Pb is approximately four times heavier than Mn, the mole % in both cases is comparable (about 15–21 mol % for Mn versus 10–24 mol % for Pb).

Effect of Mn on Particle Size. The size distribution of uraninite nanoparticles was characterized after the NaOH treatment using Fourier-filtered HRTEM images of the uraninites (Table 1). The corresponding micrographs, Fourier-filtered images, and particle size distribution histograms are shown in Figure SI-4 of the Supporting Information. The average particle size of the NaOH-treated biogenic uraninite decreases from 2.5 to 1.7 nm (± 0.15) at the higher Mn concentrations. Crystallite sizes extracted from the Rietveld refinements of the SR-PD data for varying Mn concentrations (Figure SI-5 of the Supporting Information) also exhibit this overall trend. Several explanations can be put forth for the observed trend, including Mn(II) binding to uraninite surfaces retards crystal growth or the structural strain resulting from the incorporation of Mn(II) limits particle growth.

Effect of Mn on Oxidation State and Short- and Intermediate-Range Structures of Biogenic Uraninite. U L_{III}-edge XANES spectra show the untreated Mn-reacted uraninite samples to contain 100% U(IV) within detection limits (Figure SI-8 of the Supporting Information). EXAFS spectroscopy was used to characterize the structure around U in NaOH-treated samples and around U and Mn following pH 5 washes. U L_{III}-edge EXAFS spectra, fits, and associated Fourier transforms (FTs) for NaOH-treated biogenic uraninite

are shown in Figure 1 and Table 2. The focus on NaOH-treated samples is necessary because for the untreated samples the presence of biomass-sorbed U(IV) partially obscures the signal for UO₂ (Figure SI-6A of the Supporting Information). U EXAFS data and fits for the untreated and pH 5-washed samples are presented in Figure SI-6 and Table SI-2 of the Supporting Information.

EXAFS spectra and FTs of the NaOH-treated samples qualitatively resemble those of stoichiometric UO_{2.00} (Figure 1), notably including a strong O shell at 1.8 Å ($R + dR$) (corresponding to the O shell at 2.35 Å) and a strong U shell at 3.8 Å ($R + dR$) (corresponding to the 3.85 Å U–U distance in the uraninite structure). This conclusion is consistent with the SR-PD results (Figure SI-5 of the Supporting Information), which indicate the reduction products to be uraninite. The biogenic uraninite O shell FT peaks are all unsplit, in contrast to the slightly to strongly split O shells of UO_{2.05} and UO_{2.25} (U₄O₉) (Figure 1 and ref 16). This comparison suggests the composition of biogenic uraninite is approximately UO_{2.00}. Quantitative EXAFS fits are provided in Table 2 and described in section SI-K of the Supporting Information.

The FTs show a clear effect of the presence of Mn on the structure of UO₂ (Figure 1). Comparing the Mn-free sample to the lowest Mn(II) concentration considered (0.25 mM) shows a loss of intermediate range structure (U–U shells at >4 Å) as well as a loss in amplitude of the first U–U shell at 3.82 Å (Figure 1). For Mn concentrations ranging from 0.25 to 1 mM, the qualitative effect of Mn on the FTs is similar (Figure 1), which is consistent with those samples having approximately the same Mn loading (62.9–68.7 mg Mn/g uraninite) (Table 1). At higher Mn(II) concentrations (2.5 and 5 mM), the amplitude of the U–U shell decreases again and corresponds to a concomitant increase in Mn loading that ranges from 81.6–84.1 mg Mn/g uraninite (Table 1).

TABLE 2. U L_{III} EXAFS Fit Results for NaOH-Treated Biogenic Uraninite with Varying Mn Concentration during Reduction^a

NaOH-treated uraninites							
Mn (mM)	U–O			U–U			
	<i>N</i>	<i>R</i> (Å)	$\sigma^2 \times 10^{-3}$ (Å ²)	<i>N</i>	<i>R</i> (Å)	$\sigma^2 \times 10^{-3}$ (Å ²)	$\sigma^2/N \times 10^{-3}$
5	5.5 (8)	2.352 (9)	10 (1)	5 (1)	3.82 (1)	9 (2)	1.8
2.5	6.3 (8)	2.339 (8)	12 (1)	5 (1)	3.813 (9)	9 (1)	1.8
1	6.2 (9)	2.342 (9)	9 (2)	3.6 (9)	3.819 (8)	5 (1)	1.4
0.5	5.6 (8)	2.338 (9)	8 (1)	5 (1)	3.820 (9)	7 (1)	1.4
0.25	6.1 (6)	2.350 (6)	9.2 (9)	4.4 (8)	3.828 (6)	6.7 (9)	1.5
0	6.9 (8)	2.334 (7)	10 (1)	6 (1)	3.835 (6)	7.3 (8)	1.2

^a Values in parentheses are fit-derived 1 sigma uncertainties in the last reported digit. The no Mn sample also included three additional U–U shells at distances fit to 5.42(2), 6.70(3), and 7.57(3) Å; coordination numbers fixed at 6, 24, and 12; and the Debye-Waller factor fixed at 0.006, 0.008, and 0.004 Å⁻², respectively.

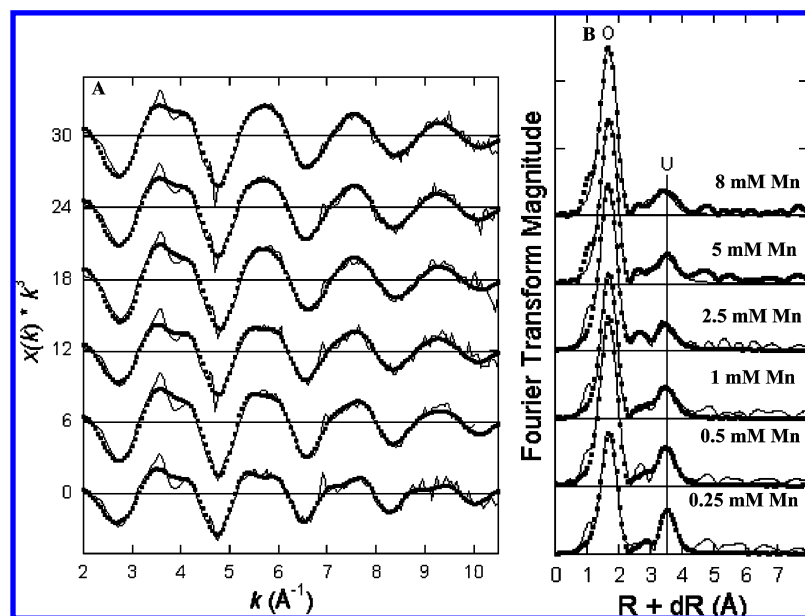


FIGURE 2. (A) Mn K-edge EXAFS and (B) Fourier transforms of pH 5-washed, Mn-reacted uraninite. Solid lines represent data, and dotted lines represent the fits to the data. Fits were performed over the *k* range from 4 to 10 Å⁻¹ to avoid contamination from the multielectron excitation feature at about 3.5 Å⁻¹. The obtained fits are overlaid on top of experimental data below 4 Å⁻¹ to show the good agreement between the model and observed spectra.

This progression indicates a stepwise increase in Mn concentration and a stepwise decrease in the amplitude of the U–U shell, which is due to an increase in disorder. The smaller U–U shell amplitudes indicate loss of structural order as Mn(II) loading increases, implicating a structural mechanism of internal U binding.

Local Structure around Mn²⁺. K-edge EXAFS analyses were performed to investigate the local structure around Mn(II). Mn²⁺ sorbs readily to biomass and uraninite surfaces, necessitating its removal by NaOH treatment and subsequent pH 5 washing in order to spectroscopically isolate structurally bound Mn(II). EXAFS spectra, FTs, and fits of the pH 5-washed samples are shown in Figure 2 and Table 3. Mn XANES spectra indicate the samples to be 100% Mn(II) (Figure SI-7 of the Supporting Information). Furthermore, the Mn K-edge EXAFS qualitatively resemble those of the U L_{III}-edge, particularly at the lowest Mn(II) concentration (Figures 1 and 2); both feature two prominent FT frequencies, one at about 1.8 Å and another at 3.5–3.8 Å (*R* + *dR*). This observation suggests that Mn and U have similar near-neighbor geometries, qualitatively supporting the idea that some fraction of internally bound Mn occupies U sites.

In the Mn K-edge EXAFS FT, the large peak at about 1.8 Å (*R* + *dR*) corresponds to an average of 4.6 O atoms (Table 3). The 2.16 Å fit-derived Mn–O distance is consistent with

TABLE 3. Mn K-Edge EXAFS Fit Results for pH 5-Washed Mn-Reacted Biogenic Uraninite Samples^a

Mn (mM)	pH 5 washed and NaOH-treated uraninites					
	Mn–O			Mn–U		
	<i>N</i>	<i>R</i> (Å)	$\sigma^2 \times 10^{-3}$ (Å ²)	<i>N</i>	<i>R</i> (Å)	$\sigma^2 \times 10^{-3}$ (Å ²)
8	4.1 (7)	2.17 (1)	9 (2)	N.R.	3.67 (4)	N.R.
5	4.7 (6)	2.156 (9)	8 (1)	N.R.	3.68 (4)	N.R.
2.5	5.3 (9)	2.15 (1)	9 (2)	N.R.	3.65 (6)	N.R.
1	4.1 (7)	2.15 (1)	7 (2)	7 (5)	3.67 (4)	25 (9)
0.5	5.4 (9)	2.15 (1)	9 (1)	6 (4)	3.65 (3)	21 (8)
0.25	4.1 (7)	2.17 (1)	9 (2)	4.3 (2)	3.67 (3)	16 (5)

^a Values in parentheses are fit-derived 1 sigma uncertainties in the last reported digit. N.R. = not reported (see text).

octahedral Mn²⁺–O (18–20). However, the low CN (i.e., 4.6 versus 6) indicates that Mn(II) is not in an ideal octahedron and has static disorder (as indicated by a split shell) that cannot be resolved by the FT and is not captured by the Debye–Waller term. Such behavior is common in layered Mn oxides (21) and obscures the true CN. If four Mn–O bonds have lengths of 2.16 Å (and bond valence of 0.37 v.u.

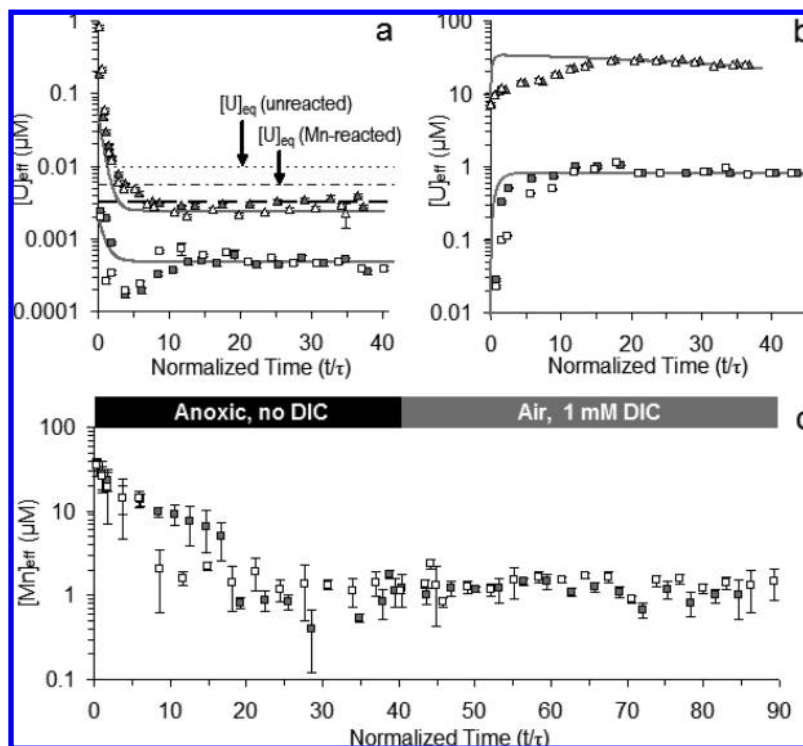


FIGURE 3. (a,b) Effluent concentration of dissolved uranium as a function of normalized time (t/τ , residence time $\tau \sim 6$ min) in flow-through dissolution experiments using NaOH-treated, biogenic UO_2 unreacted (Δ , \blacktriangle) and 5 mM Mn-reacted (\square , \blacksquare). Neither sample was washed at pH 5. Duplicates are shown by open and filled symbols. Error bars reflecting 95% confidence intervals of analytical results are sometimes hidden by the symbols. (a) Reducing, carbonate-free conditions. Thin dotted lines indicate the experimentally determined equilibrium concentration, $[\text{U}]_{\text{eq}}$, while the thick dashed line represents the $[\text{U}]_{\text{eq}}$ of amorphous UO_2 calculated from the NEA-TDB (26). (b) Oxidizing conditions in presence of air-equilibrated feed solution containing 1 mM carbonate. Solid gray lines illustrate the modeled response based on calculated dissolution rate constants. (c) Effluent concentration of dissolved manganese under both experimental conditions, switched from reducing to strongly oxidizing after about 40 residence times.

each), then the remaining Mn–O bonds must have a total valence of 0.52 v.u. to obtain a required bond valence sum of 2 v.u. (22). This requirement is satisfied by 2 Mn–O bonds of with average distances of 2.29 Å or 3 Mn–O bonds with distances of 2.44 Å. Because both values are within the general range of U–O distances for UO_{2+x} , we conclude that Mn may be either 6 or 7 coordinated.

The second-neighbor FT peak at about 3.5 Å ($R + dR$) becomes asymmetric, broader, shorter, and shifted to lower R with increasing initial $[\text{Mn}(\text{II})]$. In these uraninites, Mn is approximately 6-fold less abundant than U (Table 1) and undersaturated with respect to Mn (hydr-)oxides and carbonate formation. Hence, the second-shell frequency can be ascribed to U neighbors but with Mn likely to be present at a lower relative abundance to form a mixed U/Mn shell. The increasing asymmetry and broadening of the second-shell peak in response to increasing $[\text{Mn}(\text{II})]$ is qualitatively consistent with a mixed U/Mn shell that incorporates more Mn in response to rising solution concentration. In this case, the term, “mixed shell” is defined operationally to include atomic subshells that may lie at distinct distances but are too close to be resolved by the data. Fits to the Mn EXAFS (Figure 2) were obtained for the ≤ 1 mM $[\text{Mn}(\text{II})]$ samples and indicated the presence of 4 to 7 U neighbors at about 3.66 Å. The systematic and rapid increase in Mn–U σ^2 with escalating $[\text{Mn}(\text{II})]$ (Table 3) may be attributed to the presence of Mn substituting for U or the presence of an unresolved and growing Mn–Mn shell. Because no other phases were detected by SR-PD (Figure SI-5 of the Supporting Information), it is reasonable to posit that these shells are components of a common host phase.

The distortion and asymmetry of the second shell are sufficiently large in the >1 mM $[\text{Mn}(\text{II})]$ samples that fits

using a symmetric disorder parameter (σ^2) produce physically unrealistic fit results; N and σ^2 obtain values as high as 15 atoms and 0.04 \AA^2 (and for this reason are not reported in Table 2). The data do not permit a multishell analysis of the broadened second-shell frequency (i.e., to fit an additional Mn or U shell), and we do not know the functional form of the atomic distribution. Thus, no further quantitative analysis is presented other than to indicate that the shells lie in the vicinity of 3.67 Å. It is notable that a corresponding trend of increasing second-shell peak breadth was not observed in the U L_{III} -edge EXAFS. An explanation is that Mn tends to substitute next to itself in the structure, and thus, the impact of increasing Mn incorporation disproportionately impacts the Mn K-edge EXAFS. We propose that there is preferential incorporation of Mn in the outer region of the UO_2 nanoparticles, which is consistent with (a) that region having greater structural disorder (16) and (b) the incorporation mechanism of cations in nanoparticles being driven by sorption to nanoparticle (23).

Effect of Mn on Uraninite Reactivity. The oxidation of geological uraninite is inhibited by the presence of mono- and divalent cation impurities and nonstoichiometry (10). By analogy, lower reactivity of Mn-reacted biogenic uraninite could be expected due to the incorporation of Mn^{2+} cations. The reactivities of 5 mM Mn-reacted and unreacted biogenic uraninite (both NaOH-treated) were compared by evaluating their respective dissolution in the presence and absence of oxygen. Unreacted uraninite dissolved significantly and reproducibly faster than 5 mM Mn-reacted uraninite in the presence and absence of O_2 (Figure 3). Calculated average dissolution rates for unreacted and Mn-reacted uraninite, respectively, in $\text{mol U m}^{-2} \text{ s}^{-1}$ for anaerobic conditions were 3.4×10^{-13} versus 1.2×10^{-14} and for aerobic conditions

were 1.0×10^{-9} versus 2.6×10^{-11} . Thus, the stability of Mn-reacted uraninite is higher than that of the unreacted uraninite by a factor of 28 and 38, when contrasting anaerobic and aerobic conditions.

Furthermore, the equilibrium uranium concentration as determined from the reactor run in the batch SBR mode (thin dotted lines in Figure 3a) was lower for the Mn-reacted uraninite (5.5×10^{-9} M) than that for the unreacted uraninite (9.5×10^{-9} M), which is consistent with lower solubility for the Mn-reacted solid.

The measured effluent Mn concentration in the oxic portion of the dissolution experiment is $\sim 1 \mu\text{M}$. On the basis of the congruent dissolution of Mn-substituted uraninite, the expected concentration should be about $0.4 \mu\text{M}$ because the U:Mn molar ratio is 2.4 for the sample considered. The measured effluent Mn concentration is $\sim 1 \mu\text{M}$. Calculations (section SI-J of the Supporting Information) reveal that only $\sim 18\%$ of the sorbed Mn(II) is removed over the 90 residence times of the experiment, while less than 1% of the total uraninite is dissolved during that time. Thus, we suggest that the effluent Mn(II) concentration actually corresponds to the concentration of aqueous Mn(II) in equilibrium with Mn(II) sorbed onto the uraninite surface. This finding implies that sorbed Mn(II) may contribute to the stability of Mn-reacted uraninite. Nonetheless, analogous observations of increased stability of Mn-reacted uraninite were obtained in batch dissolution studies subjected to an additional treatment (pH 5 wash) to strip off sorbed Mn (Figure SI-9 of the Supporting Information). While we cannot exclude the possibility that sorbed Mn contributes to the observed phenomenon, the structural changes resulting from Mn incorporation into uraninite appear to improve the stability of the Mn-reacted mineral.

The results suggest that Mn-reacted uraninite is more resistant to oxidation than unreacted uraninite due to greater thermodynamic stability and slower rates of surface-mediated processes. It is notable that the Mn-reacted uraninite displays slower oxidation when compared to unreacted uraninite despite its smaller particle size (Table 1) and presumably higher surface area. Furthermore, there is a potential for chemical oxidation of Mn(II) by O_2 at the dissolution pH of 7.5 (24). Both factors could accelerate oxidative dissolution rather than retard it, making the observed stability of Mn-reacted uraninite all the more remarkable. The conclusion that Mn-reacted uraninite is less soluble and more resistant to dissolution than unreacted uraninite is consistent with the reported increase in stability conferred by impurities to geological uraninites [8,10,11]. A recent study of the effect of Ca^{2+} on biogenic uraninite has shown that contrary to Mn^{2+} , this cation does not affect the kinetics of uraninite oxidation (25).

Mn(II) Binding Site. Three aqueous chemical observations strongly imply that Mn(II) is structurally bound within the solid particles: (a) Up to 4.4 wt % Mn(II) remains associated with the particles after NaOH and repeated washes at pH 5, conditions under which surface-sorbed Mn(II) is readily removed. (b) The amount of Mn(II) remaining bound to uraninite after washing is about 6-fold higher than can be sorbed onto preformed Mn-free uraninite at pH 6.5 (data not shown). (c) The equilibrium solubility of Mn-reacted uraninite is half that of Mn-free uraninite (in spite of the smaller particle size of the former), indicating a lower free energy and hence thermodynamic alteration of particle identity.

At the highest Mn(II) concentrations, uraninite exhibits a lattice contraction (Figure SI-5 of the Supporting Information), which suggests incorporation of the smaller Mn^{2+} cation into the uraninite lattice. The EXAFS Mn–U CN value (e.g., 4 U atoms in the 0.25 mM Mn sample) also suggests incorporation of Mn within the uraninite structure. Specif-

ically, the observed Mn–U distance of about 3.67 \AA is slightly shorter than the U–U distance and suggests substitution of Mn^{2+} onto uranium sites, which could result in local structural contraction around Mn. Substitution of Mn(II) on the interstitial sites would require Mn–U distances of about 2.73 and 4.74 \AA , which are not observed.

Key questions that follow from this conclusion are how to reconcile the Mn^{2+} coordination polyhedron with the cubic uranium site and how to maintain charge balance. Substitution of Mn^{2+} for U^{4+} must be compensated by loss of oxygens, the presence of higher-valent uranium, or other coupled substitutions such as incorporation of H^+ . The XANES spectra show no evidence for systematic increases in U valence with increasing [Mn(II)] (Figure SI-8A of the Supporting Information). However, the loss of one oxygen for each Mn(II) incorporated would produce a distorted heptahedron (Figure SI-10 of the Supporting Information) that would be consistent with the lower Mn–O CN in the Mn K-edge EXAFS results. It would also reduce the U–O CN from 8 to 7 for the three other (U) atoms that were bonded to the excised O atom. Thus, at the highest observed Mn content (4.4 wt %, equivalent to about 19% of the U sites), the average U–O CN value would drop to about 7.4. Unfortunately, this prediction cannot be independently verified from the U EXAFS because the deviation from 8 is comparable to the uncertainties of the fit-derived U–O CN values. This model is thus consistent with all of the observations and suggests a unit-cell formula of $\text{U}_x\text{Mn}_{(1-x)}\text{O}_{(1+x)}$.

Implications for U(VI) Bioremediation. The remediation of U(VI)-contaminated groundwater through the microbial reduction of U(VI) and the production of uraninite, where it occurs, will unavoidably take place in the presence of divalent cations, including relatively high concentrations of Mn(II). Under the conditions considered, this work suggests that Mn(II) incorporation into uraninite at lattice positions confers increased stability to biogenic uraninite. By extension, one can expect that other divalent groundwater solutes may exhibit similar interactions with biogenic uraninite. This observation suggests a previously unappreciated paradigm for biogenic uraninite, one in which the reactivity of the material is closely related to bulk geochemical conditions in the surrounding environment.

Acknowledgments

We thank Steve Conradson for providing U_4O_9 ; Carol Morris, Ray Russ, Darryl Murray, Joe Rogers, Jeff Maske, and Ron Marks for technical assistance; Jean-David Teuscher and Michael Bensimon at EPFL for use of the ICP-OES and HR-ICP-MS; Kerry Kreitman and Scott Dixon at WUSTL for help in the laboratory and in modeling. Funding was provided by Swiss NSF Grant 20021-113784 and U.S. Department of Energy, Office of Basic Energy Sciences Grant DE-FG02-06ER64227 and Project SCW0041. SSRL is a U.S. national user facility operated by Stanford University on behalf of the U.S. DOE-OBER. Portions of this project were supported by the DOE-BER-funded SSRL ERSP and the DOE-BER and NIH-NCRR-funded SSRL Structural Molecular Biology Program. We acknowledge CIME (EPFL) for use of the HRTEM and staff help.

Supporting Information Available

Detailed description of material preparation, experimental setup, modeling approach, material characterization, and structural model (10 figures and 2 tables). This material is available free of charge via the Internet at <http://pubs.acs.org>.

Literature Cited

- 1) Renshaw, J. C.; Lloyd, J. R.; Livens, F. R. Microbial interactions with actinides and long-lived fission products. *C.R. Chim.* **2007**, *10* (10–11), 1067–1077.

- (2) Bargar, J.; Bernier-Latmani, R.; Giammar, D. E.; Tebo, B. M. Biogenic uraninite nanoparticles and their importance for uranium remediation. *Elements* **2008**, *4* (6), 407–412.
- (3) Senko, J. M.; Kelly, S. D.; Dohnalkova, A. C.; McDonough, J. T.; Kemner, K. M.; Burgos, W. D. The effect of U(VI) bioreduction kinetics on subsequent reoxidation of biogenic U(IV). *Geochim. Cosmochim. Acta* **2007**, *71* (19), 4644–4654.
- (4) Moon, H. S.; Komlos, J.; Jaffe, P. R. Uranium reoxidation in previously bioreduced sediment by dissolved oxygen and nitrate. *Environ. Sci. Technol.* **2007**, *41* (13), 4587–4592.
- (5) Komlos, J.; Mishra, B.; Lanzirotti, A.; Myneni, S. C. B.; Jaffe, P. R. Real-time speciation of uranium during active bioremediation and U(IV) reoxidation. *J. Environ. Eng.* **2008**, *134* (2), 78–86.
- (6) Senko, J. M.; Istok, J. D.; Suflita, J. M.; Krumholz, L. R. In situ evidence for uranium immobilization and remobilization. *Environ. Sci. Technol.* **2002**, *36* (7), 1491–1496.
- (7) Senko, J. M.; Mohamed, Y.; Dewers, T. A.; Krumholz, L. R. Role for Fe(III) minerals in nitrate-dependent microbial U(IV) oxidation. *Environ. Sci. Technol.* **2005**, *39* (8), 2529–2536.
- (8) Finneran, K. T.; Housewright, M. E.; Lovley, D. R. Multiple influences of nitrate on uranium solubility during bioremediation of uranium-contaminated subsurface sediments. *Environ. Microbiol.* **2002**, *4* (9), 510–516.
- (9) Allen, G. C.; Tempest, P. A. Ordered defects in the oxides of uranium. *Proc. R. Soc. London, Ser. A* **1986**, *406* (1831), 325–344.
- (10) Finch, R. J.; Ewing, R. C. The corrosion of uraninite under oxidizing conditions. *J. Nucl. Mater.* **1992**, *190*, 133–156.
- (11) Janeczek, J.; Ewing, R. C. Structural formula of uraninite. *J. Nucl. Mater.* **1992**, *190*, 128–132.
- (12) Janeczek, J.; Ewing, R. C. Dissolution and alteration of uraninite under reducing conditions. *J. Nucl. Mater.* **1992**, *190*, 157–173.
- (13) *Final Environmental Assessment of Groundwater Compliance at the New Rifle, Colorado, UMTRA Project Site*; U.S. DOE-EA-1406; U.S. Department of Energy: Washington, DC, 2003.
- (14) Integrated Field-Scale Subsurface Research Challenge. <http://www.esd.ornl.gov/orifrc/index.html>, U.S. Department of Energy Oak Ridge site groundwater composition data.
- (15) Shannon, R. D.; Prewitt, C. T. Effective ionic radii in oxides and fluorides. *Acta Crystallogr.* **1969**, *B25*, 925–946.
- (16) Schofield, E. J.; Veeramani, H.; Sharp, J. O.; Suvorova, E.; Bernier-Latmani, R.; Mehta, A.; Stahlman, J.; Webb, S. M.; Clark, D. L.; Conradson, S. D.; Ilton, E. S.; Bargar, J. R. Structure of biogenic uraninite produced by *Shewanella oneidensis* strain MR-1. *Environ. Sci. Technol.* **2008**, *42* (21), 7898–7904.
- (17) Brooks, S. C.; Fredrickson, J. K.; Carroll, S. L.; Kennedy, D. W.; Zachara, J. M.; Kelly, S. D.; Kemner, K. M.; Fendorf, S. Inhibition of bacterial U(VI) reduction by calcium. *Environ. Sci. Technol.* **2003**, *37* (9), 1850–1858.
- (18) Jarosch, D. Crystal structure refinement and reflectance measurements of Hausmannite, Mn₃O₄. *Mineral. Petrol.* **1987**, *37* (1), 15–23.
- (19) Christensen, A. N. A single crystal X-ray diffraction study of Mn(OH)₂. *Acta Chem. Scand.* **1965**, *19* (7), 1765–8.
- (20) Effenberger, H.; Mereiter, K.; Zemann, J. Crystal structure refinements of magnesite, calcite, rhodocrosite, siderite, smitsonite, and dolomite with discussion of some aspects of the stereochemistry of calcite type carbonates. *Z. Kristallogr.* **1981**, *156* (3–4), 233–243.
- (21) Webb, S. M.; Tebo, B. M.; Bargar, J. R. Structural characterization of biogenic Mn oxides produced in seawater by the marine *Bacillus* sp strain SG-1. *Am. Mineral.* **2005**, *90* (8–9), 1342–1357.
- (22) Brese, N. E.; Okeeffe, M. Bond-valence parameters for solids. *Acta Crystallogr., Sect. B: Struct. Sci.* **1991**, *47*, 192–197.
- (23) Erwin, S. C.; Zu, L.; Hatfel, M. I.; Efros, A. L.; Kennedy, T. A.; Norris, D. J. Doping semiconductor nanocrystals. *Nature* **2005**, *436*, 91–94.
- (24) Chinni, S.; Anderson, C. R.; Ulrich, K. U.; Giammar, D. E.; Tebo, B. M. Indirect UO₂ oxidation by Mn(II)-oxidizing spores of *Bacillus* sp strain SG-1 and the effect of U and Mn concentrations. *Environ. Sci. Technol.* **2008**, *42* (23), 8709–8714.
- (25) Burgos, W. D.; McDonough, J. T.; Senko, J. M.; Zhang, G. X.; Dohnalkova, A. C.; Kelly, S. D.; Gorby, Y.; Kemner, K. M. Characterization of uraninite nanoparticles produced by *Shewanella oneidensis* MR-1. *Geochim. Cosmochim. Acta* **2008**, *72* (20), 4901–4915.
- (26) Guillaumont, R.; Fangänel, T.; Fuger, J.; Grenthe, I.; Neck, V.; Palmer, D. A.; Rand, M. H. *Update on the Chemical Thermodynamics of Uranium, Neptunium, Plutonium, Americium, and Technetium*; Elsevier: Amsterdam, 2003; Vol. 5, p 970.

ES900556K